Research Article

Sebastian J. Muderspach**, Tobias Tandrup**, Kristian E. H. Frandsen, Gianluca Santoni, Jens-Christian N. Poulsen, Leila Lo Leggio*

Further structural studies of the lytic polysaccharide monooxygenase *Ao*AA13 belonging to the starch-active AA13 family

Abstract: Lytic polysaccharide monooxygenases (LPMOs) are recently discovered copper enzymes that cleave recalcitrant polysaccharides by oxidation. The structure of an *Aspergillus oryzae* LPMO from the starch degrading family AA13 (*Ao*AA13) has previously been determined from an orthorhombic crystal grown in the presence of copper, which is photoreduced in the structure. Here we describe how crystals reliably grown in presence of Zn can be Cu-loaded post crystallization. A partly photoreduced structure was obtained by severely limiting the X-ray dose, showing that this LPMO is much more prone to photoreduction than others. A serial synchrotron crystallography structure was also obtained, showing that this technique may be promising for further studies, to reduce even further photoreduction. We additionally present a triclinic structure of *Ao*AA13, which has less occluded ligand binding site than the orthorhombic one. The availability of the triclinic crystals prompted new ligand binding studies, which lead us to the conclusion that small starch analogues do not bind to *Ao*AA13 to an appreciable extent. A number of disordered conformations of the metal binding histidine brace have been encountered in this and other studies, and we have previously hypothesized that this disorder may be a consequence of loss of copper. We performed molecular dynamics in the absence of active site metal, and showed that the dynamics in solution differ somewhat from the disorder observed in the crystal, though the extent is equally dramatic.

Keywords: LPMO; starch degradation; photoreduction; substrate binding; molecular dynamics.

Abbreviations

AA, auxiliary activities; *An*AA13, lytic polysaccharide monooxygenase from *Aspergillus nidulans*; *Ao*AA13, lytic polysaccharide monooxygenase from *Aspergillus oryzae*; CAZy, Carbohydrate Active enZyme database; CBM, carbohydrate binding module; LPMO, lytic polysaccharide monooxygenase; MD, molecular dynamics; *Mo*LPMO13A, lytic polysaccharide monooxygenase from *Magnaporthe oryzae*; *Nc*AA13, lytic polysaccharide monooxygenase from *Nerospora crassa*; PDB, Protein Data Bank; PEG, polyethylene glycol; RMSD, root mean square deviation; SSX, serial synchrotron crystallography; *Ta*AA9A, lytic polysaccharide monooxygenase from *Thermoascus aurantiacus*.

1 Introduction

Lytic polysaccharide monooxygenases (LPMOs) are enzymes capable of boosting the degradation of recalcitrant polysaccharides, such as cellulose, chitin and starch (as reviewed in, e.g., [1-3]). They are metalloenzymes which, utilizing a single copper ion active-site in conjunction with external electron donors and molecular oxygen or hydrogen peroxide as co-substrates, have been observed to cleave the glycosidic bond oxidatively [2,4]. LPMOs are classified as auxiliary activities (AA) in the Carbohydrate Active enZymes database (CAZy) [5] and are to date differentiated into seven families: AA9, AA10, AA11,

*Corresponding author: Leila Lo Leggio, Department of Chemistry, University of Copenhagen, 2100 København Ø, Denmark, E-mail: leila@chem.ku.dk
Sebastian J. Muderspach, Tobias Tandrup, Kristian E. H. Frandsen, Jens-Christian N. Poulsen, Department of Chemistry, University of Copenhagen, 2100 København Ø, Denmark
Gianluca Santoni, ESRF, Structural Biology Group, 71 avenue des Martyrs, 38027 Grenoble cedex, France
**These authors contributed equally to the work

AA13, AA14, AA15 and AA16. AA14, AA15 and AA16 are all recently discovered [6-8], while the rest have been known for some time. Similar for all LPMOs is the active site, which consists of two histidines, one being the N-terminal residue. The two histidines form the so-called histidine brace that coordinates the active copper ion [9]. This study focuses on *Aspergillus oryzae* AA13 (*Ao*AA13), which is part of the starch degrading family. This family has not received as much attention as the chitinolytic/cellulolytic AA9-AA11 families. The AA13 family was first described in Harris and Wogulis [10] as a family of polypeptides enhancing starch degradation, but it was not recognised as an LPMO until Vu et al. [11] described the activity of an AA13 from *Neurospora crassa* (*Nc*AA13). In 2015 the first structure of an AA13 family member was determined [12]. The structure was of *Ao*AA13 (from *Aspergillus oryzae*). No activity could be detected for *Ao*AA13 but the synergetic activity of the highly related *Aspergillus nidulans* AA13 (*An*AA13) with β-amylase on retrograded corn starch could be shown [12].

*An*AA13 and *Ao*AA13 are very similar in sequence (72% identity) and presumably structure, but *An*AA13 is also associated with a family 20 carbohydrate binding module (CBM20). CBM20 is a family of starch-specific binding modules associated with many starch degrading enzymes including amylases, and most often C-terminally positioned with respect to the catalytic domains [13], and they are present in approximately 60% of all AA13 sequences known to date. The first quantitative data of binding affinity for an AA13 enzyme containing CBM20 was published by Nekiunaite et al. [14]. The binding affinity for *Magnaporthe oryzae* LPMO13A (*Mo*LPMO13A) on insoluble wheat starch granules and *Aspergillus terreus* LPMO13A (*At*LPMO13A) on β-cyclodextrin was comparable to CBM20-containing hydrolases, suggesting a very similar function and structure/function relationship for CBM20 in both hydrolytic and oxidative enzymes, namely to aid catalysis by increasing proximity to the substrate. Accordingly, the relationship among CBM20 sequences followed taxonomy rather than whether they were appended to hydrolytic or oxidative enzymes [14]. *Ao*AA13 possible ability to bind starch related substrates was further investigated by Frandsen et al. [15], who published ligand-bound crystal structures, however, they had uncertain biological relevance.

The active site of the *Ao*AA13 consists of a copper ion coordinated by the histidine brace with an additional tyrosine as a more distant axial ligand. The catalytically crucial N-terminal histidine is methylated as is often observed for fungal LPMOs, but the purpose for this methylation is still unknown though some experiments with *Thermoascus aurantiacus* AA9A (*Ta*AA9A) indicate

it may protect the enzyme from oxidative damage [16]. According to current proposals of LPMO action, in the resting state of the enzyme the copper is in a copper(II) state and can coordinate to up to six ligands in a more or less distorted octahedral coordination, depending on the enzyme [2]. In this state the *Ao*AA13 is presumably coordinated twice to the methylated histidine (MeHis1) once each to His91 and Tyr224 and two water molecules. Due to photoreduction in the X-ray beam, the copper in LPMOs is often reduced to copper(I) during the data collection, and therefore it expels the exogenous ligands to end up in a T-shape coordination as observed in the crystal structure of *Ao*AA13 [2,12].

In all structures of *Ao*AA13 so far, the active-site copper is either reduced to Cu(I) or substituted by Zn. Here we attempt to obtain a crystal structure in the resting state for *Ao*AA13. Crystals produced for this study are in the previously described $P2_12_12_1$ crystal form [12] grown in the presence of Zn. Since crystals cannot be reliably obtained in the presence of Cu, a robust procedure for exchanging the metal had to be developed first. As carefully reducing the X-ray dose and using helical data collection did not lead to a predominantly Cu(II) structure, we tested the possibility of using serial synchrotron crystallography (SSX) to reduce the effect of radiation [17], which seems to be promising for further studies.

Furthermore, we present a new *P*1 crystal form of *Ao*AA13, which has a much more open putative substrate binding site. Unfortunately, attempts to obtain oligosaccharide complexes with this new crystal form were not successful. In fact, there is so far to our knowledge no direct evidence that AA13 domains bind oligosaccharides.

During crystallographic studies of *Ao*AA13 presented here and previously we have encountered remarkable plasticity of the active site, which has been found in a number of conformations, for example while searching for oligosaccharide binding, a structure with an *Ao*AA13 was determined where one of the active-site histidines is 'flipped' completely out of its normal metal binding position [15]. We have therefore additionally explored the active site of *Ao*AA13 by molecular dynamics (MD) simulations.

2 Materials and method

2.1 Crystallization and metal exchange

A batch of the endoH deglycosylated *Ao*AA13 enzyme was produced as in previous studies (provided by Novozymes

A/S) and stored in 20 mM MES pH 6.0 and 125 mM NaCl at 4 °C [10,12].

The crystals used for the low X-ray dose studies were grown in conditions based on previously reported crystallization [12] using the hanging drop vapour diffusion method with a reservoir consisting of 0.1 M buffer II pH 5.0 (0.2 M L-malic acid, 0.4 M MES, 0.4 M Tris) [18], 0.2 M Zn-acetate and 19-23% polyethylene glycol (PEG) 3000. The 4 μL hanging drop was set up by hand in a VDX plate (Hampton Research) and contained protein solution (6 mg/mL) and reservoir in a 3:1 ratio. The crystals were grown to full size in 3 days at room temperature. The crystals were then transferred in fibre loops to a soaking drop containing 22.5% (w/v) PEG 3000, 0.09 M buffer (II) pH 5.0, 0.5 mM Cu-acetate and 1 mg/mL bovine serum albumin. A few small crystals were transferred to satiate the solution before the crystals intended for data collection were transferred. The crystals were soaked for 10 min and mounted on fibre loops to be frozen in liquid nitrogen. No cryoprotectant was needed for the crystal. The method was quite tolerant of small variations in soaking times and concentrations of components.

Crystals used for SSX were grown using the same procedure as above. Crystals intended for the SSX experiment were grown to a size of 25 μm in each dimension. Crystals were harvested using mesh LithoLoops (Molecular Dimensions). Before flash freezing, a paper wick (MiTeGen) was taken to the underside of the mesh LithoLoop in order to remove excess liquid and allow the crystals to adhere to the surface of the mesh LithoLoop.

The protein stock solution of the glycosylated form of *Ao*AA13 (in 20 mM Tris, 50 mM NaCl at pH 9.0) was concentrated to 24 mg/mL. Crystalline plates were obtained in a PACT screen (B12 condition: 0.01 M $ZnCl_2$, 20% (w/v) PEG 6000, 0.1 M MES, pH 6.0) [19] using the sitting drop vapour diffusion method in a MRC 2-drop plate (Molecular Dimensions) set up by an Oryx8 robot (Douglas Instruments). The crystals were reproducible with seeding in 14-20% (w/v) PEG 6000 with 17-24 mg/mL protein in VDX plates using the hanging drop vapour diffusion method (1000 μL reservoir, 4 μL drop size, and 1:1 ratio of protein:reservoir). The crystal used for structure determination was grown with 0.01 M $ZnCl_2$, 14% (w/v) PEG 6000, 0.1 M MES, pH 6.0, and 30% (v/v) glycerol was used as cryoprotectant for flash freezing in a cryo-loop.

Later, the same crystal form (isomorphous and with similar plate morphology) was obtained under the standard conditions for the *deglycosylated* protein as stated above, by adding 15 μL Milli-Q water to a drop with already obtained crystals (this procedure was carried out in an attempt to obtain bigger crystals). The crystals dissolved due to the decrease in protein concentration and recrystallized in a few days with a very slight increase in size but also with formation of crystals of different morphology (plates). The reference plate crystals were mounted on fibre loops for data collection without Cu-acetate soak.

2.2 Oligosaccharide crystal soaks

Both metal-exchanged $P2_12_12_1$ crystals and $P1$ plate crystals obtained during the recrystallization experiment were used for oligosaccharide soaking. To the regular Cu-acetate soak a final concentration of 500 mM maltose or 50 mM maltopentaose was added for the $P2_12_12_1$ crystals and they were soaked for at least 10 minutes. For the plate crystals ($P1$) either 50 mM maltopentaose or 50 mM β-cyclodextrin were added to the regular Cu-acetate soak and the crystals were soaked for at least 10 minutes. No cryoprotectant was needed prior to flash freezing in cryo-loops.

2.3 Data collection and processing

All data were collected at cryotemperature (100 K). The lowest dose data were collected on ID23-1 [20] beamline at the ESRF using reduced transmission and helical data collection [21]. The crystal was rotated 100° in steps of 0.1° while translating 45.5 μm along the crystal. Later, data from the same crystal were obtained on P11 at Petra III (DESY) [22] from collection at wavelengths of 1.00 Å and 1.35 Å for verification of the metal exchange. Data on a reference crystal were collected on ID23-1 at ESRF. The data were processed using the XDS program [23]. The average diffraction weighted dose for these and the SSX data below was calculated using Raddose3D [24].

SSX data sets were collected at beamline ID29 [25] at the ESRF using the *mesh and collect* routine [26]. Data were collected with a wavelength of 0.98 Å over 10° of total rotation with an oscillation of 0.1° per image at each of the crystals identified using the routine. The data sets were processed individually with identical parameters using XDS [23], using the first processable data set as a reference. The hierarchical cluster analysis software ccCluster [27] was initially used to determine, which data sets could be merged based on their pairwise correlation coefficient. It was, however, found that processing statistics were suboptimal after scaling using XSCALE [23]. We chose to merge all processable data sets and scale together. Data sets with an R-factor in the innermost shell above 20% were excluded from the scaling. All data sets

mentioned above (conventional data collection and SSX) belonged to the space group $P2_12_12_1$, in which the structure was originally solved.

X-ray crystallographic data of the glycosylated form of *Ao*AA13 were collected at I911-2 at the MAX-IV synchrotron in Lund, Sweden. The data could be processed in $P1$ with two molecules in the asymmetric units. Plate crystals of deglycosylated *Ao*AA13 grown by recrystallization and used for oligosaccharide soaks were isomorphous to the $P1$ crystals of the glycosylated form. Data presented for the recrystallized $P1$ crystals were collected at ID23-1 at ESRF. Other crystal tests for this project were carried out at P11, Desy, Hamburg, ESRF beamlines or MAX IV Biomax beamline.

Data collection statistics are presented in Table 1 for deposited structures (lowest dose *Ao*AA13 Cu-bound structure, $P1$ glycosylated *Ao*AA13 structure and SSX *Ao*AA13 Zn-bound structure) and Table S1 (other collected data).

2.4 Structure determination, refinement and validation

The CCP4 suite was used for structure determination and refinement [28]. Structures of metal exchanged *Ao*AA13 crystals (and corresponding reference crystal) as well as low X-ray dose structures and SSX structure were phased by difference Fourier methods. The first glycosylated *Ao*AA13 structure in $P1$ was phased by Molecular Replacement in Molrep [29] with the preliminary *Ao*AA13 structure used for phasing in [12] as search model. Oligosaccharide soaks in isomorphous crystals were subsequently phased by difference Fourier methods. All structures were refined in REFMAC5 [30] alternated with cycles of manual rebuilding in Wincoot [31].

We chose to deposit only structures, which gave new information compared to others in the Protein Data Bank (PDB), namely the lowest dose *Ao*AA13 Cu-bound structure, $P1$ glycosylated *Ao*AA13 structure and SSX *Ao*AA13 Zn-bound structure. For the deposited structures, refinement and validation statistics and PDB deposition codes are in Table 1. For other structures that have been partly or fully refined, refinement and validation statistics are in Table S1.

2.5 Thermal shift assay

A thermal shift assay was conducted using a Tycho NT.6 nano differential scanning fluorimetry instrument.

To the *Ao*AA13 sample copper acetate was added in stoichiometric amounts compared to the LPMO. Several potential ligands were tested to see if they would cause a shift in inflection temperature, which could indicate binding in solution. Maltose, maltopentaose, maltoheptaose and β-cyclodextrin (Sigma-Aldrich) as well as isomaltotriose, 6^3-α-D-glucosyl-maltotriose, and 6^3-α-D-glucosyl-maltotriosyl-maltotriose (Megazymes) were dissolved separately in the same buffer as the protein (stated in section 2.1). *Ao*AA13 and the oligosaccharide solutions were mixed to obtain final concentrations of 0.2 mg/mL enzyme and 30-50 mM oligosaccharide and tested on the nano differential scanning fluorimetry instrument.

2.6 MD simulations

The MD simulations were performed in GROMACS 2016 [32] with the CHARMM36 force field [33]. The PDB file (code: 4OPB) was stripped of ions (including the active site copper ion), ligands and water molecules and inserted into a cubic box (7.46 nm in each direction from the centre of the protein molecule). As GROMACS did not have an entry for the methylated histidine, a normal histidine was used instead in the N-terminal position. 12871 SPC/E modelled water molecules were added to the box and the *Genion* subprogram in GROMACS was used to identify the charge of the protein and 20 Na$^+$ ions were added to stabilize this charge. To avoid steric clashes, the system was relaxed by energy minimization using the steep minimization algorithm with a maximum of 50000 steps and termination when maximum force obtained a value below 1000 kJ/mol/nm. Afterwards, the system was equilibrated in NVT equilibration at 300 K using Berendsen thermostat and NPT equilibration using 300 K and 1.0 bar. Four simulations were run in total, two simulations of 10 ns (see Figure S2) and two of 40 ns, all using 1 fs timesteps with identical parameters, except for deviating thermal noise obtained by a random number generator.

Results of the MD simulations were analysed using GROMACS subprograms *rmsf* and *rmsdist* to calculate the deviation per residue over an entire simulation, and the average deviation of the whole protein molecule throughout the simulation, respectively. Additionally, the Python library Biopython [34] was used to extract the root mean square deviation (RMSD) at each time point of the simulation (only 10 ns to 40 ns considered) of His1 and His91 against published structures 4OPB and 5T7K, and the SSX structure from this study.

Table 1: Data collection, processing and refinement statistics for deposited structure.[a]

	Low dose Cu*Ao*AA13	SSX *Ao*AA13 (Zn)	Glycosylated *Ao*AA13 (Zn)
PDB code	6TBQ	6TC4	6TBR
Wavelength (Å)	1.30	0.98	1.04
Space group	$P2_12_12_1$	$P2_12_12_1$	$P1$
a,b,c (Å)	46.31, 61.32, 72.98	46.72, 61.43, 73.78	46.06, 49.76, 57.10
Alpha, beta, gamma (º)	90, 90, 90	90, 90, 90	109.4, 90.1, 95.5
Resolution range (Å)	7.68-1.72 (1.76-1.72)	50.0-2.0 (2.05-2.00)	20.00-1.70 (1.74-1.70)
Completeness (%)	99.1(88.4)	97.5 (97.3)	92.6 (91.2)
R(meas) (%)	33.2 (232.7)	42.4 (238.6)	7.7 (45.5)
CC½(%)	98.7 (42.5)	92.2 (42.4)	99.4 (87.7)
Signal to noise [$I/\sigma(I)$]	4.6(0.6)	4.91 (1.87)	2.87 (9.04)
Total no. of reflections	36678 (2701)	59240 (4374)	81477 (5750)
No. of unique reflections	9725 (758)	14527 (1066)	48576 (3521)
R(work) (%)	22.05	18.52	19.17
R(free) (%)	26.33	22.25	24.64
No. of non-H atoms			
Protein	1829	1817	1838/1870[b]
Metal ions	6	13	12
Water	163	179	533
Total	1998	2009	4253
Average B factor (Å²)			
Protein	25.2	15.17	17.43/17.22[b]
Ion	47.7	52.59	20.40
Water	30.7	25.45	27.81
RMSD bond length (Å)	0.011	0.010	0.019
RMSD angles (º)	1.44	1.34	1.85
Ramachandran plot			
Most favoured (%)	96.04	94.81	95.7
Allowed (%)	3.52	4.33	3.8

[a] Values for the outer shell is given in the parentheses. Dynarama in Coot [31] is used to generate the Ramachandran plot.
[b] Chain A/chain B.

3 Results

3.1 Active-site metal exchange

For *Ao*AA13 no reliable crystallization procedure in the presence of copper ions has been established. The structure of *Ao*AA13 with copper at the active site has been obtained through seeding, but the procedure was not deemed reproducible [12]. It is, however, possible to reliably crystallize the enzyme in the presence of zinc-acetate solution and thereby have zinc at the active site [15]. In this paper we demonstrate that due to the high copper affinity in the active site, a soak containing copper acetate can successfully exchange the zinc ion at the active site for a copper ion in *Ao*AA13. The metal ion exchange has been done in similar fashion for *Ao*AA11 [35]. In this

paper the metal ion exchange was validated by comparing the anomalous signal at either side of the zinc absorption edge.

We expected that if Zn was successfully exchanged for Cu we would see an increase of anomalous signal in the anomalous difference map in data collected at 1.35 Å wavelength compared to 1.00 Å wavelength for a copper site. Likewise, we will see a decrease for a Zn site, given the position of the edges for the two elements are 1.284 Å for zinc and 1.381 Å for copper. Indeed the anomalous difference peak of the active-site metal increases from 12.04σ in the 1.00 Å wavelength data to 33.20σ for the 1.35 Å wavelength data, identifying it as copper, while an additional Zn binding site (between Glu125 and Asp129) shows a decrease from 5σ for the 1.0 Å data collection to less than 2σ for the 1.35 Å data collection. The signal corresponding to well-ordered sulphur atoms, for example the S in Cys25, is more or less the same (4σ) at both wavelengths. Small modifications of the metal exchange procedure still resulted in exchange for other crystals (data not shown). Unexpectedly, the reference un-exchanged structure shows a difference in conformation of the histidine brace compared to previously determined structures (discussed further below).

3.2 Low X-ray dose structure

The low X-ray dose structure received an average diffraction weighted dose of 2.57 kGy. This produced a data set with a partially photoreduced copper at the active site (Fig. 1A), where an equatorial water molecule is present 2.1 Å from the copper, but the axial water molecule is ejected completely. The B-factor for the equatorial water molecule is 36.3 Å^2, while the B-factor for the rest of the active site is roughly 20 Å^2. This indicates that not even the equatorial water molecule has full occupancy. The same crystal was afterwards exposed to 31.9 kGy (average diffraction weighted dose) and as visualized in Figure 1B, a clear difference is visible, as the equatorial water molecule is heavily depleted. For comparison, the best Zn-loaded structure (PDB code: 5T7J) in the same space group is shown in Figure 1C, while the previously published photoreduced Cu-loaded structure (PDB code: 4OPB) is shown in Figure 1D.

3.3 Structure of glycosylated *Ao*AA13 in *P*1 space group

The structure of the glycosylated form of *Ao*AA13 was solved in space group *P*1 to 1.7 Å resolution with two molecules in the asymmetric unit (Table 1), unlike the original structure, which was determined in space group *P*2$_1$2$_1$2$_1$ with one molecule in the asymmetric unit. All 233 amino acid residues were visible in the electron density, however, no glycosylation could be reliably modelled. In the structure of the glycosylated form of *Ao*AA13 both molecules adopt the immunoglobin-like β-sandwhich fold (common of LPMOs) consisting of six β-strands as well as three short α-helices (Fig. 2) and are essentially identical (RMSD of 0.10 Å over C$_\alpha$ of all residues). In addition, the structure is very similar to the *Ao*AA13 structure with active site Cu (PDB code: 4OPB) previously determined one in space group *P*2$_1$2$_1$2$_1$ (RMSD of 0.42 and 0.43 Å over C$_\alpha$ of 232 residues for chain A and B, respectively) only with some minor variations in some loops (most pronounced in loop L6; Fig. 2B). The active site is ordered (in both chain A and B) and His1, His91, Tyr224 as well as two exogenous water ligands coordinate a Zn^{2+} ion in an octahedral arrangement (metal-ligand distances of 2.0-2.4 Å and angles ranging from 83-103°).

We have previously attempted to obtain oligosaccharide ligand complexes with the orthorhombic crystals, but found that the active site is partly occluded. The crystal contacts in the *P*1 space group lead to a less occluded presumed substrate binding site compared to the *P*2$_1$2$_1$2$_1$ structure (especially compared to Zn-depleted structures; Fig. 3C middle) and thus were chosen for new oligosaccharide soaking experiments.

3.4 Serial synchrotron crystallography structure of *Ao*AA13

The structure of *Ao*AA13 could be determined by SSX through a mesh and collect procedure, and be refined to excellent R-factors and density (Fig. 4A) in the *P*2$_1$2$_1$2$_1$ space group. Surprisingly however, the (Zn-loaded) active site assumes a different conformation than seen previously (Fig. 4B). However, this conformation was also observed in a reference Zn structure used to demonstrate metal exchange, so it is not a consequence of the method, but could be a consequence of sample aging. In fact, it was noticed that crystals grown in this period were smaller than originally observed earlier in the project. However, and very puzzlingly, in the recrystallized *P*1 crystals also grown in this period (Table S1), the active site is in its
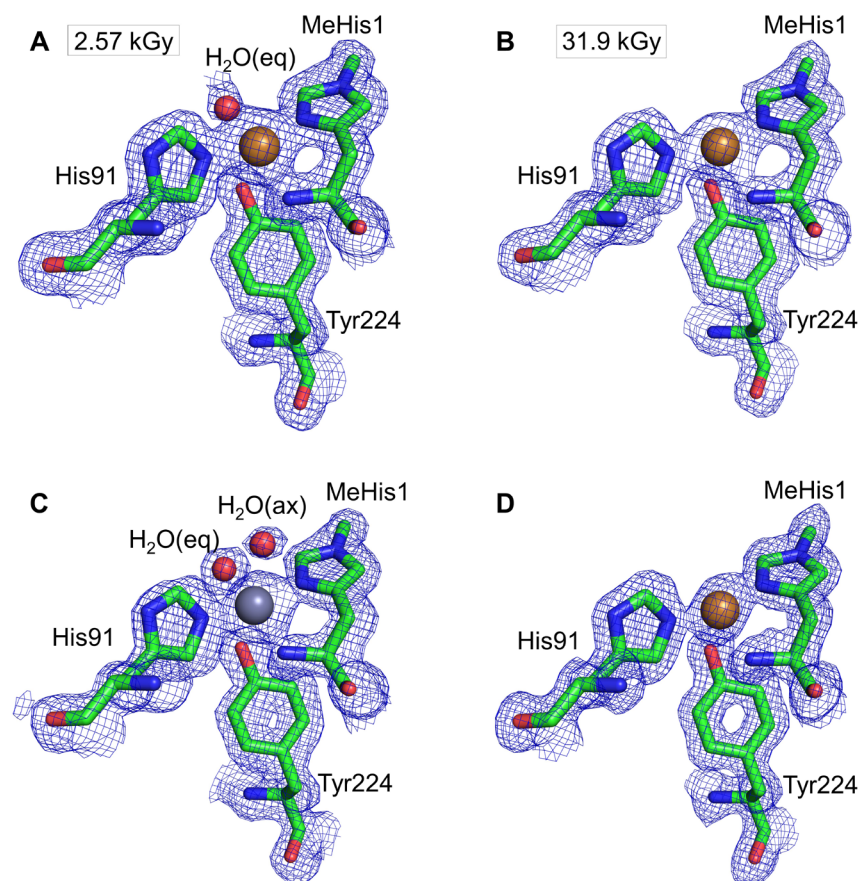
Figure 1: Structure of the active site in different structures of *Ao*AA13. (A) The low dose, partly photoreduced Cu-loaded structure from this manuscript; (B) the same crystal exposed to a higher dose being fully photoreduced; (C) Zn-loaded structure (PDB code: 5T7J) [15]; (D) previous copper loaded structure (PDB code: 4OPB) [12] exhibiting a fully photoreduced copper ion. The maps are weighted 2Fo-Fc electron density maps contoured at the 1 σ level.
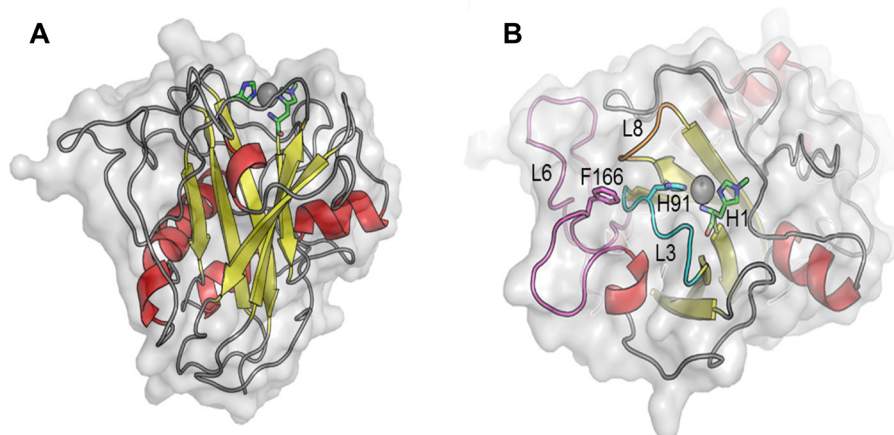

Figure 2: Chain A of the glycosylated form of *Ao*AA13 in space group *P*1. Part (A) shows a side view, whereas part (B) shows a top view with marking of the flexible loops around the active site histidine brace. Loops separating secondary structure elements are numbered in accordance with their appearances in the sequence. Loops marked L3 (cyan), L6 (magenta) and L8 (orange) are equivalent to loop L3, LC and L8 in AA9 LPMOs ([1] and references therein), respectively, and correspond to the loop between β2 and β3, the long loop preceding β4, and the loop between β5 and β6 in [12]. In both (A) and (B) α-helices and β-strands are colored red and yellow, respectively.
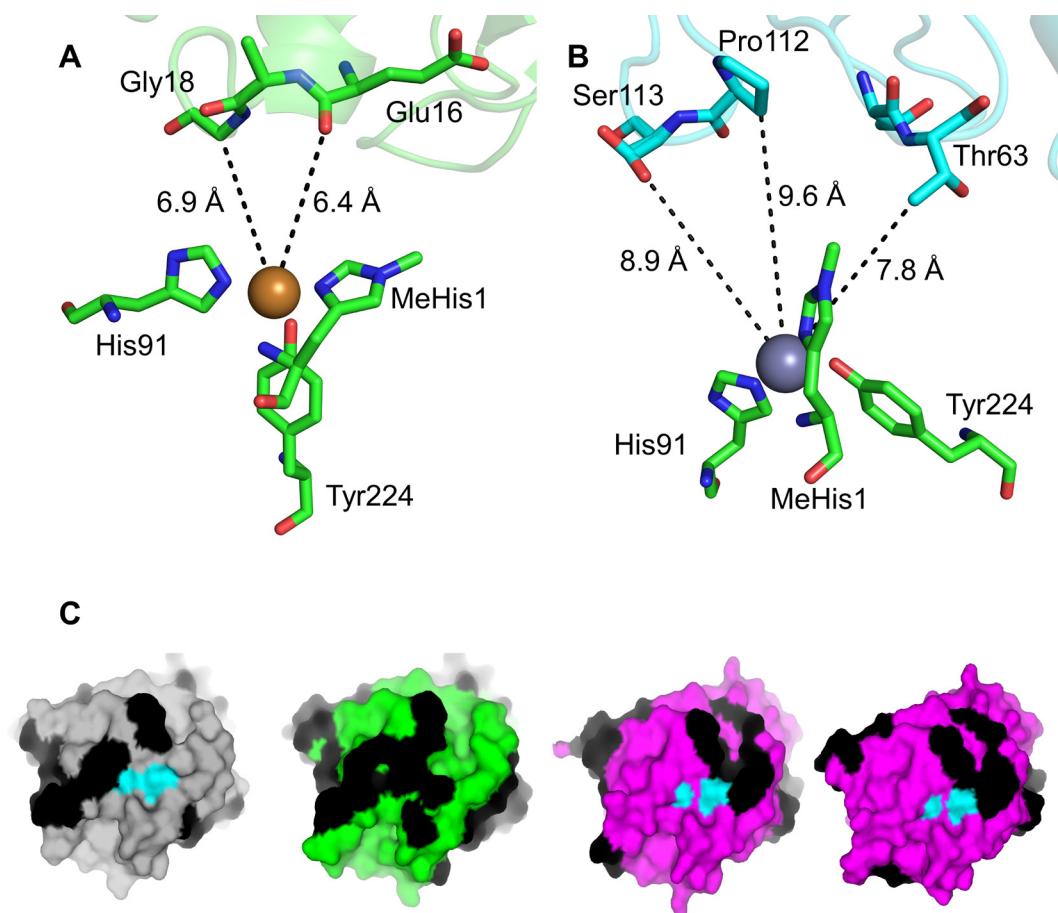
Figure 3: Crystal packing and active site occlusion. (A) The active site in the $P2_12_12_1$ space group, with distances to the closest symmetry related molecule. (B) The active site in the $P1$ space group with some distances to the closest symmetry related molecule. (C) Orthorhombic form of *Ao*AA13 (grey). The *Ao*AA13 after soak with maltose (green) in absence of Zn in shown in the middle, whereas the $P1$ structure of *Ao*AA13 chain A and B (magenta) is shown on the right. Crystal contacts are shown in black and the histidine brace is shown in cyan.

usual geometry (Fig. 4C). The average diffraction weighted dose received by the SSX structure is estimated to be 0.175 kGy in Raddose3D, calculated based on the dose received by a single crystal.

3.5 Ligand binding experiments

We have previously attempted to obtain crystal complexes of *Ao*AA13 in the orthorhombic crystal form by soaking crystals in different maltooligosaccharides with a degree of polymerization ranging between 2 and 7 in Zn-depleted conditions and by cocrystallization (degree of polymerization 5). Thus initially, the rational for the metal exchange experiments was to stabilize the active site, as we had observed disorder in the previous oligosaccharide soaks in absence of Cu, which had been attributed to active-site metal depletion during the soaks.

It was hypothesized that this induced small structural changes, which led to additional active-site occlusion in the crystal [15]. In the course of the present work we have observed, however, that some crystals where Zn has successfully exchanged with Cu nonetheless had a more occluded binding site. As such our previous conclusions seem incorrect and the slightly more or less open active site in the orthorhombic crystals does not have a simple explanation.

Soaking of a metal-exchanged orthorhombic crystal (open active site) with 0.5 M maltose did not result in complex formation (results not shown), which argues for the published complex with maltose (PDB code: 5LSV) [15] being primarily an artifact of crystal contacts. No other complexes could be obtained with this crystal form (see section 2.2).

Since the $P1$ crystal form is more open, it was used for additional ligand binding experiments with some of the
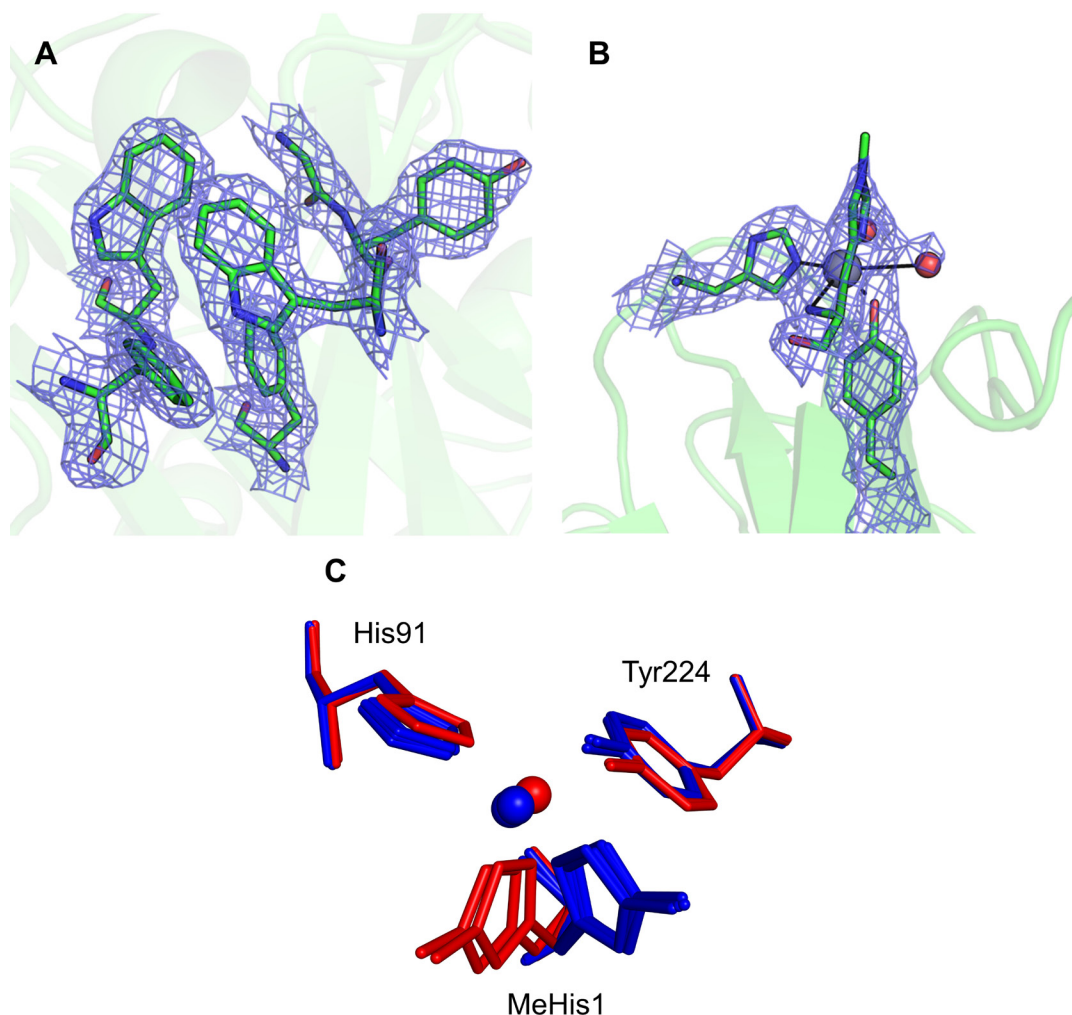
Figure 4: SSX structure. (A) Electron density in protein core; (B) electron density at histidine brace. (C) The histidine brace and supporting Tyr224. The previously published copper-loaded structure (PDB code: 4OPB), the most well-ordered Zn-loaded structure (PDB code: 5T7J), glycosylated *Ao*AA13 in *P*1 (Zn-loaded, this manuscript), *P*1 recrystallization structure (Zn-loaded, this manuscript) are all depicted in blue, while the SSX structure (orthorhombic, this manuscript) and the reference Zn-*Ao*AA13 (orthorhombic, this manuscript) are depicted in red.

larger ligands. The *P*1 crystal form can be obtained from the glycosylated form of the *Ao*AA13, or, by recrystallization, with the deglycosylated form of the protein. As the crystals of the glycosylated form have relatively high mosaicity (0.598°), we chose to use the recrystallized form (mosaicity of 0.162° for the reported data set; Table S1). β-Cyclodextrin as well as maltopentaose were tested (section 2.2) but no crystal complex could be obtained (results not shown).

In order to probe binding in solution, we used native differential scanning fluorimetry to test if several possible ligands showed sign of substrate-enzyme interactions by inducing a shift in melting temperature, but this was not the case with the ligands tested (see section 2.5) at the given concentrations.

3.6 Active-site conformations in crystals and in solution

A number of different conformations have been observed for the active-site histidines of *Ao*AA13: (1) well-ordered, canonical LPMO active-site conformations; (2) the conformations in the disordered active sites in [15]; and (3) the conformation observed for the $P2_12_12_1$ Zn-crystals in this study (Fig. 4C in red). As all structures of LPMOs with a highly occupied copper site show conformations similar to (1), we were curious to see if MD simulations in solution, upon removal of the copper, would show transition of the active sites to conformations similar to the disordered ones observed in (2) and (3). Thus we chose as the start of
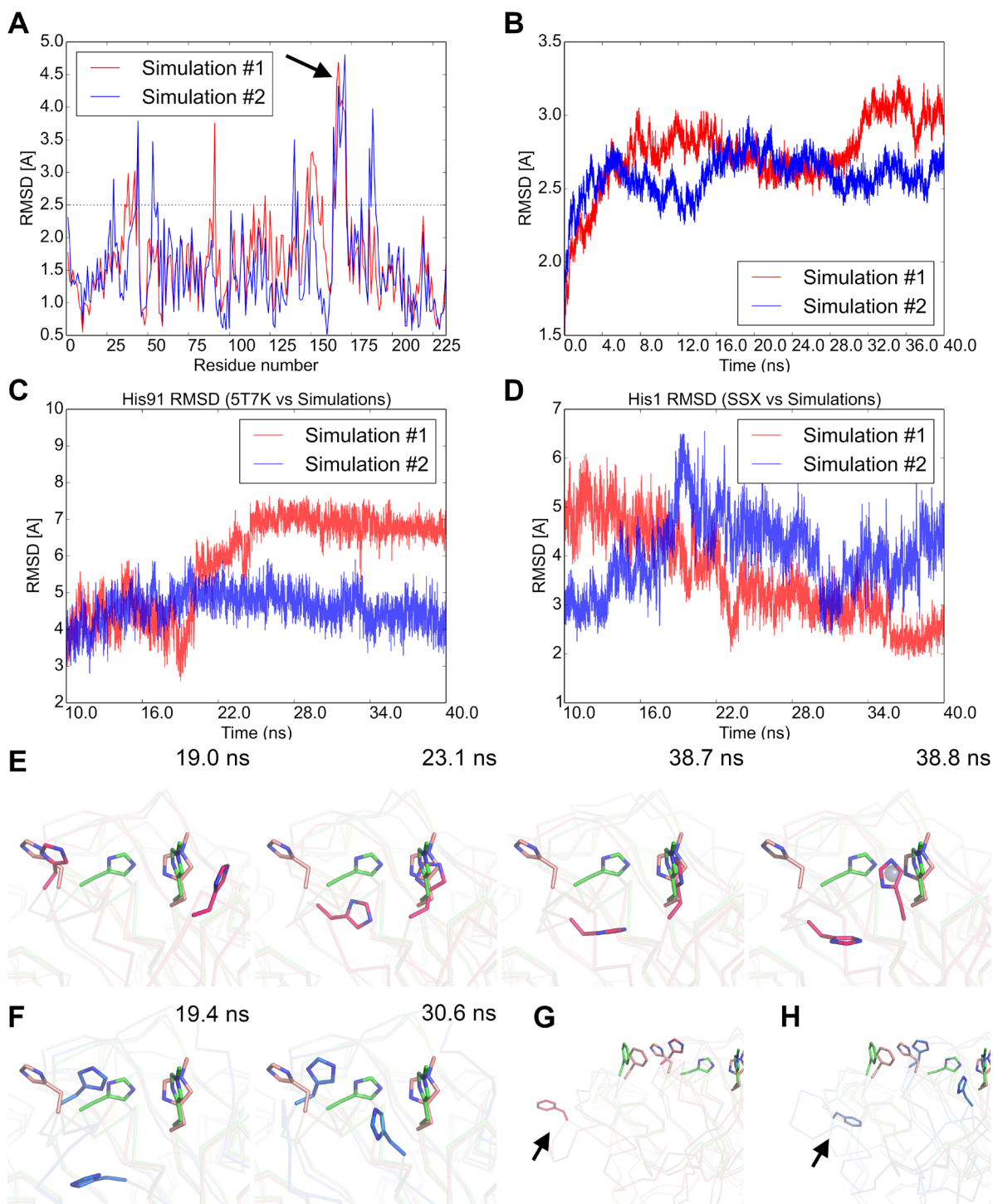
Figure 5: Forty ns MD simulations of *Ao*AA13. (A) RMSD of side chains after superimposing C$_\alpha$'s of all frames in simulation compared to the first frame of the simulation. Residues above an RMSD of 0.25 Å are listed in Table S3. Residue Phe166 is indicated with a black arrow. (B) Average coordinate RMSD throughout each 40 ns simulation. In order to identify steps in the MD simulation reproducing the disorder seen in the crystal structures, RMSD of His91 was calculated against that of the *Ao*AA13-Hisflip structure (PDB code: 5T7K) published in [15] (C), while RMSD of the N-terminal histidine against that of the SSX structure (D) using Biopython [34]. (E) and (F) They show selected conformations of interest in simulations 1 and 2, respectively, as mentioned in the text. The His91 conformations shown in (F) are representative of all conformations adopted throughout simulation 2, as reflected in (C). (G) and (H) They show the general conformation of Phe166 (indicated with black arrow) in both simulations, respectively. Simulation 1 is shown in red, simulation 2 in blue, the structure with the PDB code 5T7K in tan, and the SSX structure in green.

our simulation the well-ordered Cu-loaded structure (PDB code: 4OPB) after stripping it of the metal ion.

Figures 5A and 5B show the side chain RMSD from starting structure per residue (over a 40 ns simulation), and for the whole protein over time, respectively. Loop L6 (refer to Figure 2 for notation) containing Phe166 was particularly mobile, much more so than the regions containing the active-site histidines. In simulation 1 (Fig. 5G) Phe166 flips quickly to an outward position and remains solvent exposed for the rest of the simulation. In simulation 2 after equilibration Phe166 packs against a loop, but is still very distant from the active site (Fig. 5H). While Phe166 has been modelled in alternate and somewhat different conformations in the various crystal structures, none of these conformations are so distant from the active site. The two active-site histidines show mobility in the MD simulations, but not to the same extent (Fig. 5A,C,D). In particular, the large His91 'flip', which is observed in the published structure with PDB entry 5T7K [15], is mostly not observed in either simulations (Fig. 5C), though some conformations are close (e.g., at 19.0 ns in simulation 1; Fig. 5E). We interpret this as a consequence of the mobility of the L6 loop bearing Phe166 in solution, moving this residue further away from the active site and thus diminishing the possibility for the stabilizing interaction with a 'flipped' His91 side chain as seen in the 5T7K crystal structure. Instead, His91 tended to bury itself and seemingly interact with other residues from the L3 loop and Tyr224 (Fig. 5E at 23.1, 38.7 and 38.38 ns), or position itself in between the usual conformation and the 'flipped' conformation (Fig. 5F). His1 also tended to move towards the position normally occupied by the metal ion (e.g., Fig. 5E at 38.8 ns), furthermore the imidazole group often flipped 90° resembling somewhat the conformation observed in the SSX structure and the reference Zn-AoAA13 structure in this work (e.g., Fig. 5E at 38.7 ns).

4 Discussion and conclusions

In this study we present a successful and verified procedure for exchanging the active-site metal from Zn to Cu in orthorhombic crystals of AoAA13, which has been used for further studies.

A number of structures of AoAA13 have been previously presented, mostly with Zn at the active site, as for example PDB code: 5T7J, which presents a well-ordered active site. In the only copper-loaded structure available (PDB code: 4OPB), the copper is presumably photoreduced to Cu(I). It is likely that the geometry around the Zn represents a Cu(II) state quite closely. On the other hand, several of the Zn-loaded structures we presented in the past show some disorder of the active site.

Thus we sought to obtain a low dose X-ray crystal structure of AoAA13, as previously obtained for other AA9 and AA10 LPMOs [36-38]. The structure presented here obtained by limiting the dose by beam attenuation, short exposures and helical data collection shows a partly photoreduced active site, with clear density for the equatorial ligand. The average diffraction weighted dose received was 2.57 kGy for this data set, while a dose of 31.9 kGy is sufficient for full photoreduction. It is not easy to compare this dose directly to the doses reported for EfAA10A crystals, since an earlier version of RADDOSE was used. It is, however, likely that the doses reported by Gudmundsson et al. [36] are either the maximum dose or the average dose for the exposed volume, which for the low/higher dose AoAA13 structures presented here are 5.67/5.07 kGy and 70.2/62.9 kGy, respectively. For the least photoreduced structure of EfAA10A (PDB code: 4ALC) the dose is reported as 82.7 kGy, which corresponds well to a Cu(II) form. Thus at much lower doses than adequate to maintain a Cu(II) state for EfAA10A, AoAA13 is clearly photoreduced. For LsAA9A, a fully photoreduced structure has never been obtained. This clearly indicates that AoAA13 is much more susceptible to photoreduction than other LPMOs, which perhaps can be correlated to its unusual electron paramagnetic resonance spectrum, where hyperfine coupling is visible in the absence of oligosaccharide ligands, unlike other LPMOs [12].

The geometries at the active site for well-ordered Zn-loaded structures, low dose structure and Cu(I) structure are shown in Table S2. The distances to histidine ligands are typical of other LPMOs. The Tyr-metal distances are somewhat shorter for the well-ordered Zn-loaded structures than the Cu-loaded structures, while the distance to the water ligands slightly longer than to the partly photoreduced Cu-loaded structure. In terms of θ_1, θ_2 and θ_3, the well-ordered Zn structures are closer to the Cu(II) geometry, while both Cu-structures are closer to Cu(I) geometry [2].

We additionally determined a (Zn-loaded) structure by SSX to see if the approach could eventually be used for obtaining a Cu(II) structure, since in this method only few degrees are collected on each of many small crystals. Since the dose can be reduced by at least one order of magnitude, and the structure has a reasonable quality, the SSX approach could be attempted in the future after metal exchange. Perhaps together with the use of very short wavelengths, a Cu(II) structure of AoAA13 can be obtained in this way.

This study presents also the structure of a glycosylated *Ao*AA13 structure crystallized in the *P*1 space group with two molecules in the asymmetric unit, with a well-ordered Zn containing active site. This *P*1 crystal form could be obtained by recrystallization in drops containing already formed orthorhombic crystals. Several ligand binding experiments were conducted in the crystals, in both orthorhombic and triclinic crystal form, but no crystal structure with substrate ligand bound was obtained, even though the putative substrate binding groove is much more open in the *P*1 structure.

In addition, no shift of thermal inflection point was observed in solution with several putative ligands, providing no additional evidence that *Ao*AA13 binds soluble substrates. It should be noted that lack of binding cannot be alone concluded by the thermal shift experiments as substrate binding does not guarantee a change in inflection point. Activity has not been demonstrated for this particular LPMO, but the presumed binding surface near the active site is highly conserved in this family (Fig S1; sequences analyzed with the ConSurf server [39]). In the last stages of completion of this manuscript, a detailed study of substrate preference of two AA13 LPMOs, one naturally with and one without CBM, has been published [40]. Based on the pattern of degradation and computational docking using the structure of *Ao*AA13 (the only one still available for this family), the authors suggest that maltooctaose may be the minimal substrate and furthermore suggest that the preferred substrate is an amylose double helix. Absence of CBM considerably reduced binding. Lack of CBM in *Ao*AA13, as well as the fact that the putative ligands tested here are smaller than the suggested minimal length, could provide an explanation for our negative crystallographic and thermal shift assay results. Furthermore, as more LPMO-like proteins are identified with low or non-detectable polysaccharide degradation activity [41], and since AA13 oxidative activity on starch has been also notoriously difficult to detect, it could be that the family AA13 members, though clearly linked to starch degradation as elegantly demonstrated by proteomic studies in *A. niger* [42], may have other primary functions than just biomass breakdown.

The SSX structure turned out to have a different geometry of the active site, which was the same as in the Zn-loaded orthorhombic structure used as reference for metal exchange, but very puzzlingly, different from the structure of the same sample after recrystallization in *P*1 space group. For the distorted SSX Zn site, the distance to the tyrosine ligand is also unusually short. Apart from already discussed consequences as possible result of sample aging [15] and consequences for storage of LPMOs, this is an additional example of active-site plasticity.

In order to further probe this plasticity, MD simulations were conducted with a metal deprived structure. This was done to see if conformations observed in the crystal could be observed in the simulations, especially an extreme 'flip' of His91, one of the histidine brace histidines. Surprisingly, while we did not observe a flip of His91 during most of the simulation, we observed instead that Phe166, with which the 'flipped' His91 interacts in crystal structures, is flipped quickly out of its usual position in the crystal structures (Fig. 5G,H). According to the simulations, Phe166 sits in a very flexible loop between β-strand 3 and 4 (loop L6; Fig. 2B), and after 10 ns both this loop and the adjacent loop bearing His91 (loop L3; Fig. 2B) have considerably different conformation than in the crystal structures. Loop L3 has identical conformations in all AA13 crystal structures determined, because its movement is restricted by crystal contacts. Because loop L3 packs against loop L6, it also is restricted in the crystal structure. In contrast the loop separating β-strand 5 and 6 (loop L8 in Figure 2B, previously denoted loop β5-β6 in [12]) clearly shows high variability in the crystal structures.

Since Phe166 cannot flip out away from the active site in the crystal, alternative motions are observed in the crystal in response to loss of metal binding. Interestingly, Phe166 marks the beginning of the 'variable substrate interaction region' in the most recent article on AA13 [40], which almost perfectly coincides with the most flexible part of the structure in both simulations (residues 166-170) and thus these dynamics are likely to be of functional importance. A recent study of dynamics of LPMOs [43] by the computationally cheaper Elastic Network Model method, identified two different regions of correlated dynamics in *Ao*AA13 (residues 206-213 and 213-221). The differences may be due to the different timescales probed by the different methods.

In conclusion, this paper presents advances in the methodology for detailed structural analysis of the starch-active family of LPMOs, AA13, and in the understanding of how their dynamics may affect their function.

S.J.M., J.N.P, T.T., K.E.H.F. and L.L.L. are members of ISBUC Integrative Structural Biology at the University of Copenhagen (http://www.isbuc.ku.dk). We thank Elspeth Garman and Joshua Dickerson for helpful discussions on the use of RADDOSE3D.

Conflict of interest: The author declares no conflict of interest.

References

[1] Tandrup T., Frandsen K.E.H., Johansen K.S., Berrin J.G., Lo Leggio L., Recent insights into lytic polysaccharide monooxygenases (LPMOs), *Biochem. Soc. Trans.*, 2018, 46, 1431–1447. https://doi.org/10.1042/BST20170549

[2] Vu V.V., Ngo S.T., Copper active site in polysaccharide monooxygenases, *Coord. Chem. Rev.*, 2018, 368, 134–157. https://doi.org/10.1016/j.ccr.2018.04.005

[3] Vaaje-Kolstad G., Forsberg Z., Loose J. S. M., Bissaro B., Eijsink V. G. H., Structural diversity of lytic polysaccharide monooxygenases, *Curr. Opin. Struct. Biol.*, 2017, 44, 67–76. https://doi.org/10.1016/j.sbi.2016.12.012

[4] Walton P.H., Davies G., On the catalytic mechanisms of lytic polysaccharide monooxygenases, *Curr. Opin. Chem. Biol.*, 2016, 31, 195–207. https://doi.org/10.1016/j.cbpa.2016.04.001

[5] Lombard V., Golaconda Ramulu H., Drula E., Coutinho P.M., Henrissat B., The carbohydrate-active enzymes database (CAZy) in 2013, *Nucleic Acids Res.*, 2014, 42, D490–D495. https://doi.org/10.1093/nar/gkt1178

[6] Couturie M., Ladeveze S., Sulzenbacher G., Ciano L., Fanuel M., Moreau C., et al., Lytic xylan oxidases from wood-decay fungi unlock biomass degradation, *Nat. Chem. Biol.*, 2018, 14, 306–310. https://doi.org/10.1038/nchembio.2558

[7] Sabbadin F., Hemsworth G.R., Ciano L., Henrissat B., Dupree P., Tryfona T., An ancient family of lytic polysaccharide monooxygenases with roles in arthropod development and biomass digestion, *Nat. Commun.*, 2018, 9, 756. https://doi.org/10.1038/s41467-018-03142-x

[8] Filiatrault-Chastel C., Navarro D., Haon M., Grisel S., Herpoël-Gimbert I., Chevret D., AA16, a new lytic polysaccharide monooxygenases family identified in fungal secretomes, *Biotechnol. Biofuels*, 2019, 12, 55. https://doi.org/10.1186/s13068-019-1394-y

[9] Quinlan R.J., Sweeney M.D., Lo Leggio L., Otten H., Poulsen J.C.N., Johansen K.S., et al., Insights into the oxidative degradation of cellulose by copper metalloenzyme that exploits biomass components, *Proc. Natl. Acad. Sci. USA*, 2011, 108, 15079–15084. https://doi.org/10.1073/pnas.1105776108

[10] Harris P., Wogulis M., Polypeptides having amylolytic enhancing activity and polynucleotides encoding same, Patent, 2010, WO/2010/059413

[11] Vu V.V., Beeson W.T., Span E.A., Farquhar E.R., Marletta M.A., A family of starch-active polysaccharide monooxygenases, *Proc. Natl. Acad. Sci. USA*, 2014, 111, 13822–13827. https://doi.org/10.1073/pnas.1408090111

[12] Lo Leggio L., Simmons T.J., Navarro Poulsen J.C., Frandsen K.E.H., Hemsworth G.R., Stringer M.A., et al., Structure and boosting activity of a starch-degrading lytic polysaccharide monooxygenases, *Nat. Commun.*, 2015, 6, 5961. https://doi.org/10.1038/ncomms6961

[13] Janecek S., Machovic M., Starch-binding domains in the post-genome era, *Cell. Mol. Life Sci.*, 2006, 63, 2710–2724. https://doi.org/10.1007/s00018-006-6246-9

[14] Nekiunaite L., Isaksen T., Vaaje-Kolstad G., Hachem M.A., Fungal lytic polysaccharide monooxygenases bind starch and β-cyclodextrin similarly to amylolytic hydrolases, *FEBS Lett.*, 2016, 590, 2737–2747. https://doi.org/10.1002/1873-3468.12293

[15] Frandsen K.E.H., Poulsen J.C.N., Tovborg M., Johansen K.S., Lo Leggio L., Learning from oligosaccharide soaks of crystals of an AA13 lytic polysaccharide monooxygenases: crystal packing, ligand binding and active site disorder, *Acta Crystallogr. D Biol Crystallogr.*, 2017, 73, 64–76. https://doi.org/10.1107/S2059798316019641

[16] Petrovic D.M., Chylenski P., Skaugen M., Sørlie M., Jensen M.S., Aachmann F.L., et al., Methylation of the N-terminal histidine protects a lytic polysaccharide monooxygenase from auto-oxidative inactivation, *Protein Sci.*, 2018, 27, 1636–1650. https://doi.org/10.1002/pro.3451

[17] Standfuss J., Spence J., Serial crystallography at synchrotrons and X-ray lasers, *IUCrJ*, 2017, 4, 100–101. https://doi.org/10.1107/S2052252517001877

[18] Newman J., Novel buffer systems for macromolecular crystallization, *Acta Crystallogr. D Biol Crystallogr.*, 2004, 60, 610–612 https://doi.org/10.1107/S0907444903029640

[19] Newman J., Egan D., Walter T.S., Meged R., Berry I., Jelloul M.B., et al., Towards rationalization of crystallization screening for small- to medium-sized academic laboratories: the PACT/JCSG+ strategy, *Acta Crystallogr. D Biol Crystallogr.*, 2005, 61, 1426–1431. https://doi.org/10.1107/S0907444905024984

[20] Nurizzo D., Mairs T., Guijarro M., Rey V., Meyer J., Fajardo P., et al., The ID23-1 structural biology beamline at the ESRF, *J. Synchrotron Radiat.*, 2006, 13, 227–238. https://doi.org/10.1107/S0909049506004341

[21] Flot D., Mairs T., Giraud T., Guijarro M., Lesourd M., Rey V., et al., The ID23-2 structural biology microfocus beamline at the ESRF, *J. Synchrotron Radiat.*, 2010, 17, 107–118. https://doi.org/10.1107/S0909049509041168

[22] Burkhardt A., Pakendorf T., Reime B., Meyer J., Fischer P., Stübe N., et al., Status of the crystallographic beamlines at PETRA III, *Eur. Phys J. Plus*, 2016, 131, 56. https://doi.org/10.1140/epjp/i2016-16056-0

[23] Kabsch W., XDS, *Acta Crystallogr. D Biol Crystallogr.*, 2010, 66, 125–132, https://doi.org/10.1107/S0907444909047337

[24] Zeldin O.B., Gerstel M. & Garman, E.F., Optimizing the spatial distribution of dose in X-ray macromolecular crystallography, *J. Synchrotron Radiat.*, 2013, 20, 49–57. https://doi.org/10.1107/S0909049512044706

[25] de Sanctis D., Beteva A., Caserotto H., Dobias F., Gabadinho J., Giraud T., et al., ID29: a high-intensity highly automated ESRF beamline for macromolecular crystallography experiments exploiting anomalous scattering, *J. Synchrotron Radiat.*, 2012, 19, 455–461. https://doi.org/10.1107/S0909049512009715

[26] Zander U., Bourenkov G., Popov A.N., de Sanctis D., Svensson O., McCarthy A.A., et al., *MeshAndCollect*: an automated

multi-crystal data-collection workflow for synchrotron macromolecular crystallography beamlines, *Acta Crystallogr. D Biol Crystallogr.*, 2015, 71, 2328–2343. https://doi.org/10.1107/S1399004715017927

[27] Santoni G., Zander U., Mueller-Dieckmann C., Leonard G., Popov A., Hierarchical clustering for multiple-crystal macromolecular crystallography experiments: the *ccCluster* program, *J. Appl. Crystallogr.*, 2017, 50, 1844–1851. https://doi.org/10.1107/S1600576717015229

[28] Winn M.D., Ballard C.C., Cowtan K.D., Dodson E.J., Emsley P., Evans P.R., et al., Overview of the CCP4 suite and current developments, *Acta Crystallogr. D Biol Crystallogr.*, 2011, 67, 235–242. https://doi.org/10.1107/S0907444910045749

[29] Vagin A., Teplyakov A., MOLREP: an Automated Program for Molecular Replacement, *J. Appl. Crystallogr.*, 1997, 30, 1022–1025. https://doi.org/10.1107/S0021889897006766

[30] Murshudov G.N., Vagin A.A., Dodson E.J., Refinement of macromolecular structures by the maximum-likelihood method, *Acta Crystallogr. D Biol Crystallogr.*, 1997, 53, 240–255. https://doi.org/10.1107/S0907444996012255

[31] Emsley P., Lohkamp B,. Scott W. G., Cowtan K., Features and development of Coot, *Acta Crystallogr. D Biol Crystallogr.*, 2010, 66, 486–501. https://doi.org/10.1107/S0907444910007493

[32] Abraham M.J., Murtola T., Schulz R., Páll S., Smith J.C., Hess B., Lindahl E., GROMACS: high performance molecular simulations through multi-level parallelism from laptops to supercomputers, *SoftwareX*, 2015, 1-2, 19–25. https://doi.org/10.1016/j.softx.2015.06.001

[33] Brooks B.R., Brooks C.L., Mackerell A.D., Nilsson L., Petrella R.J., Roux B., et al.*,* CHARMM: the biomolecular simulation program, *J. Comput. Chem.*, 2009, 30, 1545–1614. https://doi.org/10.1002/jcc.21287

[34] Cock P.J., Antao T., Chang J.T., Chapman B.A., Cox C.J., Dalke A., et al., Biopython: freely available Python tools for computational molecular biology and bioinformatics, *Bioinformatics*, 2009, 25, 1422–1423. https://doi.org/10.1093/bioinformatics/btp163

[35] Hemsworth G.R., Henrissat B., Davies G.J., Walton P.H., Discovery and characterization of a new family of lytic polysaccharide mono-oxygenases, *Nat. Chem. Biol.*, 2014, 10, 122–126. https://doi.org/10.1038/nchembio.1417

[36] Gudmundsson M., Kim S., Wu M., Ishida T., Momeni M. H., Vaaje-Kolstad G., et al., Structual and electronic snapshots during the transition from Cu(II) to Cu(I) metal center of a lytic polysaccharide monooxygenases by X-ray photoreduction, *J. Biol. Chem.*, 2014, 289, 18782–1879. https://doi.org/10.1074/jbc.M114.563494

[37] Frandsen K.E.H., Simmons T.J., Dupree P., Poulsen J.-C.N., Hemsworth G.R., Ciano L., et al., The molecular basis of polysaccharide cleavage by lytic polysaccharide monooxygenases, *Nat. Chem. Biol.*, 2016, 12, 298–303. https://doi.org/10.1038/nchembio.2029

[38] Simmons T.J., Frandsen K.E.H., Ciano L., Tryfona T., Lenfant N., Poulsen J.-C.N., et al., Structural and electronic determinants of lytic polysaccharide monooxygenase reactivity on polysaccharide substrates, *Nat. Commun.*, 2017, 8, 1064. https://doi.org/10.1038/s41467-017-01247-3

[39] Ashkenazy H., Abadi S., Martz E., Chay O., Mayrose I., Pupko T., Ben-Tal N., ConSurf 2016: an improved methodology to estimate and visualize evolutionary conservation in macromolecules, *Nucleic Acids Res.*, 2016, 44, 344–350, https://doi.org/10.1093/nar/gkw408

[40] Vu V.V., Hangasky J.A., Detomasi T.C., Henry S.J.W., Ngo S.T., Span E.A., et al., Substrate selectivity in starch polysaccharide monooxygenases, *J. Biol. Chem.*, 2019, 294, 12157–12166. https://doi.org/10.1074/jbc.RA119.009509

[41] Frandsen K.E.H, Tovborg M., Jørgensen C.I., Spodsberg N., Rosso M.N., Hemsworth G.R., et al., Insights into an unusual Auxiliary Activity 9 family member lacking the histidine brace motif of lytic polysaccharide monooxygenases, *J. Biol. Chem.*, 2019, 294, 17117–17130. https://doi.org/10.1074/jbc.RA119.009223

[42] Nekiunaite L., Arntzen M.Ø., Svensson B., Vaaje-Kolstad G., Hachem M.A., Lytic polysaccharide monooxygenases and other oxidative enzymes are abundantly secreted by *Aspergillus nidulans* grown on different starches, *Biotechnol. Biofuels*, 2016, 9, 187. https://doi.org/10.1186/s13068-016-0604-0

[43] Arora R., Bharval P., Sarswati S., Sen T.Z., Yennamalli R. M., Structural dynamics of lytic polysaccharide monoxygenases reveals a highly flexible substrate binding region, *J. Mol. Graphics Model.*, 2019, 88, 1–10. https://doi.org/10.1016/j.jmgm.2018.12.012